A quasi-implicit time advancing scheme for unsteady incompressible flow. Part I: Validation

Yih-Jena Jan [a],*, Tony Wen-Hann Sheu [b]

[a] *National Kaohsiung Marine University, Department of Marine Engineering, No. 482, Jhong Jhou 3rd Road, Kaohsiung 811, Taiwan*
[b] *Department of Engineering Science and Ocean Engineering, National Taiwan University, Taiwan*

Abstract

A quasi-implicit fractional-step method is presented for computing unsteady incompressible flow on unstructured grids. A non-staggered grid system is employed rather than a staggered grid system because of the simplicity and ease of extension to three-dimensional analysis. In this study, the momentum interpolation method, developed by Rhie and Chow [C.M. Rhie, W.L. Chow, Numerical study of the turbulent flow past an airfoil with trailing edge separation, AIAA J. 21 (1983) 1525–1532] and further extended by Zang et al. [Y. Zang, R.L. Street, J.R. Koseff, A non-staggered grid, fractional-step method for time-dependent incompressible Navier–Stokes equations in curvilinear coordinates, J. Comput. Phys. 114 (1994) 18–33], is applied to problems on unstructured grids to resolve the pressure oscillation problem occurring in a non-staggered grid system. An implicit time advancing scheme is used in order to remove the time step restriction and to reduce the required CPU time for problems with complex geometries. The nonlinear equations resulting from this fully implicit scheme are linearized without deteriorating the overall time accuracy. The system matrices are solved using the CG family method, known with P-BiCGSTAB, for momentum equation and P-CG for pressure Poisson equation. The present numerical method is applied to solve four benchmark problems and the results show good agreement with previous experimental and numerical results.
© 2007 Elsevier B.V. All rights reserved.

Keywords: Implicit scheme; Fractional step; CG family; Unstructured finite volume

1. Introduction

In this paper a second-order time-accurate numerical method is presented for solving the unsteady incompressible Navier–Stokes equations on unstructured grids. In the case of the structured grid, one of the most popular methods to obtain a time dependent solution for unsteady incompressible flow is a fractional-step method applied on the staggered grid system. In this type of method, a pseudo-pressure is used to correct the velocity field such that the continuity equation is satisfied at each computational time step [1]. However, in the case of the unstructured grids, the staggered grid system makes the code more complicated than that implemented in the non-staggered grid system, because in the staggered grid the control volumes for the pressure and velocity are very different from each other. Therefore, in general the non-staggered grid system is preferred to be chosen than in the staggered grid system in the case of the unstructured grid. The non-staggered grid system had been known to produce unrealistic pressure oscillations in the converged solution until Rhie and Chow [2] presented their numerical method (momentum interpolation method) for the steady flow which satisfies the mass conservation on non-staggered structured grids without resulting in artificial pressure oscillations. Later, Zang et al. [3] applied the concept of the momentum interpolation method to a fractional-step method for unsteady flow on non-staggered structured grids. This momentum

---

* Corresponding author.
  E-mail address: yjjan@mail.nkmu.edu.tw (Y.-J. Jan).

Nomenclature

A_f	outward area vector based on the $face_f$	*Greek symbols*	
P	pressure	ρ	density
St	Strouhal number	$\underline{\nabla}$	gradient operator
t	time	$\overline{\Omega_0}$	domain of $cell_0$
$\underline{U}$	velocity vector	$\|\Omega_0\|$	volume of Ω_0
$\underline{U}_f$	face velocity vector	δt	time step
u_i	velocity component along the i-direction	v	kinetic viscosity

interpolation method has been also applied to steady flow analysis on unstructured grids by a few researchers [4–6]. Kim and Choi [20] proposed a second-order time accuracy finite volume method for unsteady incompressible flow on hybrid unstructured grids. Kim and Choi [20] used the Crank–Nicolson approach of second-order time accuracy to resolve the nonlinear convection term. However, in this method, one does need to solve the x- and y-directional momentum equations simultaneously. Instead of doing so, a Crank–Nicolson method is used for linearization the convection term within the one-dimensional context. Thus it does solve the x- and y-directional momentum, respectively. It is briefly proved in later section that this approach can also yield the second-order temporal accuracy and is numerically proved in Example 1.

Unstructured grids have been mostly used with the finite element method. The finite volume method with unstructured grids has, however, become popular recently. Finite volume methods on unstructured grids have been mostly used for steady flow [4–9] but a few have been used for unsteady flow [10–14]. Miller and Wang [10] used the stream function and vorticity formulation for the two-dimensional flow. However, this method cannot be directly applied to the three-dimensional flow. Pan et al. [11] and Weiss and Smith [12] employed the artificial compressibility method, which needs a sub-iterative procedure at each computational time step and thus requires more computational efforts. Schulz and Kallinderis [13] and Chen and Kallinderis [14] used a first-order pressure correction method on "structured" non-staggered grids without using the momentum interpolation method and introduced the artificial dissipation to suppress oscillatory solutions. Therefore, an accurate and efficient numerical method for simulating unsteady flows on non-staggered unstructured three-dimensional grids should be developed.

A modified second-order time-accurate numerical method for calculating the unsteady incompressible flows on unstructured grids is presented. The momentum interpolation method similar to the method of Rhie and Chow [2] is developed in the non-staggered grid system, where the pressure and Cartesian velocity components are defined at each center of the cell and the face-normal velocities are defined at the mid-points of the corresponding cell faces to eliminate the unrealistic pressure oscillations. The

time-integration method is based on a quasi-implicit fractional-step procedure and the resulting nonlinear momentum equations are linearized in one dimension without losing the overall time accuracy. A finite volume method is used for the spatial derivative terms and the flow variables at the cell face are obtained using the pressure correction, which is independent of the cell shape. The accuracy of the present method is verified by analyzing four benchmark problems known as the decaying vortice [1,3,20], lid-driven cavity flow [15,20,21], vortex shedding flow [17,18,20,21], and backward-facing step flow [1,16,20] problems.

2. Numerical scheme and procedure

2.1. Governing equations

The governing equations for unsteady incompressible viscous flow are

$$
\begin{cases}
\rho \left[\frac{\partial \underline{U}}{\partial t} + \underline{\nabla} \cdot (\underline{U}\,\underline{U}) \right] = -\underline{\nabla} P + \underline{\nabla} \cdot \underline{\underline{\tau}}, \\
\underline{\underline{\tau}} \equiv \mu[(\underline{\nabla}\underline{U}) + (\underline{\nabla}\underline{U})^t] - \frac{2\mu}{3}\underline{\nabla} \cdot \underline{U},
\end{cases}
\tag{1}
$$

$$
\underline{\nabla} \cdot \underline{U} = 0,
\tag{2}
$$

where $\underline{\nabla}$ is the gradient operator, μ is the viscosity, and ρ is the fluid density. The above equations are cast in the dimensional form. To solve the above equations, use of SIMPLE algorithm does need the inner iterations to make the momentum and pressure correction equation to reach convergence. Then, the converged solution can be updated from the pressure correction. The updated velocity and pressure are substituted into the momentum equations until the solution is no longer needed to be updated under some criteria. This procedure constitutes the outer iterative loop. Consequently, it takes much longer computational time for getting a converged solution to satisfy the mass equation and momentum equation simultaneously at each time instant. Under this consideration, it does need a scheme to make the solution converged in an efficient manner and to ensure that the solution is accurate in comparison with the analytical solutions or other published numerical data. In this study, we modified the nonlinear

convection term by the Crank–Nicolson approach from one-dimensional sense and this concept can be incorporated into two-dimensional momentum equation. In order to prove that this scheme does not lose the overall temporal accuracy during the discretization, an analytical solution is tested to show that this approach offers the second-order time accuracy in time. To discretize the governing equations for fluid flow, the cell-centered finite volume method is selected. The reasons are as following:

  (a) All conservation principles are applied in a single control volume.
  (b) The variables are located at the center of the cell so that the mean value theorem is applicable.
  (c) A cell can accommodate a velocity at its center.
  (d) The number of surrounding cells is constant for a particular type of cell such as quadrilateral, triangular or hexahedral. As a result, the construction of the system matrix is straightforward.
  (e) Convection is suppressed for those cells with all nodes located at the wall in both finite volume and finite element based methods, whereas, it is reserved when using the cell-centered finite volume method.

The face velocity is defined at the mid-point of each cell face. The face-normal mass flow rate is defined as

$$J_f \equiv \rho \underline{U}_f \cdot \underline{A}_f, \tag{3}$$

where $\underline{U}_f$ is the face velocity located at the center of the face and $\underline{A}_f$ is outward, the normal face vector. It is noted that the value of this velocity $\underline{U}_f$ is not the averaged value from the two adjacent cells. In order to be free from the pressure oscillations due to the use of collocated, non-staggered grid layout, the momentum interpolation is introduced to give an exact face velocity in this study. Thus, the improved mass flow rate can be obtained. This particular observation will be shown in Example 2.

2.2. Numerical scheme

The time-integration method used to solve Eqs. (1) and (2) is based on the fractional-step method [1,20,21,27], where the pressure is used to correct the velocity field at each computational time step. The fully implicit time advancing scheme is shown as follows:

$$\rho \left[\frac{\underline{U}^{n+1} - \underline{U}^n}{\delta t} + \underline{\nabla} \cdot (\underline{U}\underline{U})^{n+1} \right]$$
$$= -\underline{\nabla} P^{n+1} + 0.5\mu(\nabla^2 \underline{U}^{n+1} + \nabla^2 \underline{U}^n) + \underline{F}, \tag{4}$$

δt is the size of time step. $\underline{F}$ $\left(i.e., \frac{\partial}{\partial x_j} \left(\mu \frac{\partial u_j}{\partial x_i} - \frac{2}{3} \delta_{ij} \mu \frac{\partial u_l}{\partial x_l} \right) \right)$ in Eq. (3) and will be addressed in Eq. (19) in later section. Implicit treatment of the convective and viscous terms eliminates the numerical stability restriction. Before we present the way for the approximation of nonlinear convec-

tion term, we analyze the one-dimensional equation written as

$$\rho \left[\frac{\delta u}{\delta t} + \frac{\partial}{\partial x}(uu) \right] = -\frac{\partial P}{\partial x} + \mu \frac{\partial^2 u}{\partial x^2}$$
$$\Rightarrow \rho \left[\frac{u^{n+1} - u^n}{\delta t} + \frac{\partial}{\partial x}(u^2) \right]$$
$$= -\left(\frac{\partial P}{\partial x} \right)^{n+1} + 0.5\mu \left(\left(\frac{\partial^2 u}{\partial x^2} \right)^{n+1} + \left(\frac{\partial^2 u}{\partial x^2} \right)^n \right). \tag{5}$$

It is noted that we neglect the extra term F for convenience. To linearize the convection term, a Crank–Nicolson formulation is given as shown below

$$\frac{\partial}{\partial x}(u^2) = 0.5 \frac{\partial}{\partial x}((u^2)^n + (u^2)^{n+1}). \tag{6}$$

A Taylor series expansion is made and we can have the following equation:

$$(u^2)^{n+1} = (u^2)^n + \delta t \left[\frac{\partial(u^2)}{\partial t} \right]^n + \frac{1}{2}(\delta t)^2 \left[\frac{\partial^2(u^2)}{\partial t^2} \right]^n + \cdots$$
$$\Rightarrow (u^2)^{n+1} = (u^2)^n + \left[\frac{\partial(u^2)}{\partial u} \right]^n \delta u + O(\delta t)^2$$
$$\Rightarrow (u^2)^{n+1} = (u^2)^n + 2u^n \delta u + O(\delta t)^2. \tag{7}$$

By substitution Eq. (7) into Eq. (6), we can have

$$\frac{\partial}{\partial x}(u^2) = 0.5 \frac{\partial}{\partial x}(2u^n u^n + 2u^n(\delta u)) + O(\delta t^2)$$
$$\Rightarrow \frac{\partial}{\partial x}(u^2) = \frac{\partial}{\partial x}(u^n u^{n+1}) + O(\delta t^2)$$
$$\Rightarrow \frac{\partial}{\partial x}(u^2)^{n+1} \approx \frac{\partial}{\partial x}(u^n u^{n+1}). \tag{8}$$

Based on the above simple analysis, the nonlinear convection term is linearized without losing the accuracy as following

$$\rho \left[\frac{\underline{U}^{n+1} - \underline{U}^n}{\delta t} + \underline{\nabla} \cdot (\underline{U}^n \underline{U}^{n+1}) \right]$$
$$\approx -\underline{\nabla} P^{n+1} + 0.5\mu(\nabla^2 \underline{U}^{n+1} + \nabla^2 \underline{U}^n) + \underline{F}^n. \tag{9}$$

It is also noted that the current approximation is shown to be of the second-order accuracy in time from one-dimensional sense. Kim and Choi [20] gave a complex approach in Crank–Nicolson manner and also achieved the second-order temporal accuracy. It solves the momentum equations based on the intermediate velocity simultaneously. Next, we apply a fractional-step procedure to Eqs. (2) and (9). Thus the proposed quasi-implicit time-advancement scheme can be expressed as

Present scheme:
$$
\begin{cases}
\rho\left[\frac{\widehat{U}-U^n}{\delta t} + \underline{\nabla}\cdot(U^n\widehat{U})\right] \\
\quad = -\underline{\nabla}P^n + 0.5\mu(\nabla^2\widehat{U} + \nabla^2\underline{U}^n) + \underline{F}^n, \\
\rho\left[\frac{U^*-\widehat{U}}{\delta t}\right] = \underline{\nabla}P^n, \\
\rho\left[\frac{U^{n+1}-U^*}{\delta t}\right] = -\underline{\nabla}P^{n+1} \\
\Rightarrow \left[\begin{array}{l} \nabla^2 P^{n+1} = \frac{\rho}{\delta t}\underline{\nabla}\cdot\underline{U}^*, \\ \Rightarrow \underline{U}^{n+1} = \underline{U}^* - \frac{\delta t}{\rho}\underline{\nabla}P^{n+1} \end{array}\right].
\end{cases}
\tag{10}
$$

The boundary condition for the intermediate velocity $\widehat{U}$ or U^* is simply set to the value of $\underline{U}^{n+1}$ and $\widehat{U}$ yields the second order in time step. It is proved by the equation given below

$$
\widehat{U} = \underline{U}^{n+1} + (\delta t)(\underline{\nabla}P^{n+1} - \underline{\nabla}P^n) \Rightarrow \widehat{U}
$$
$$
= \underline{U}^{n+1} + O(\delta t^2) \Rightarrow \underbrace{\widehat{U} \approx \underline{U}^{n+1}}_{\text{known as quasi-implicit}} . \tag{11}
$$

In the present study, the Courant–Friedrichs–Lewy (CFL) number is employed according to the definition given by Kim and Choi [20].

$$
\text{CFL} = \frac{\delta t}{2\|\Omega\|}\sum_f |\underline{U}_f \cdot \underline{A}_f|. \tag{12}
$$

2.3. Definition of cell-centered, collocated control volume

The domain under investigation is initially subdivided into an arbitrary number of convex polyhedrons called cells. The boundaries and vertices of these cells are referred to as the faces and nodes, respectively. The neighboring cells are defined as those which share a common face. All transport variables are at the cell centers. The cells used in the present study are known as the non-staggered cell-centered, collocated control volumes, as illustrated in Fig. 1.

2.4. The discrete scalar transport equation

The transport equation of a scalar quantity Φ can be cast into the following form by choosing the appropriate Γ and S_Φ

$$
\frac{\partial(\rho\Phi)}{\partial t} + \frac{\partial}{\partial x_i}(\rho u_i\Phi) = \frac{\partial}{\partial x_i}\left(\Gamma\frac{\partial\Phi}{\partial x_i}\right) + S_\Phi, \tag{13}
$$

Γ is the transport coefficient such as the viscosity. Φ can be the velocity component u_j. The source term S_Φ for the momentum equations contains the pressure gradient and the components of the stress tensor not included in the standard diffusion term and will be addressed in later section. An integration over the control volume Ω_0, as indicated in Fig. 1, results in the following equation:

$$
\frac{\|\Omega_0\|\rho\Phi_0^{n+1}}{\delta t} + \sum_f J_f\Phi_f = \sum_f D_f + \left(S_\Phi + \frac{\rho\Phi_0^n}{\delta t}\right)\|\Omega_0\|, \tag{14}
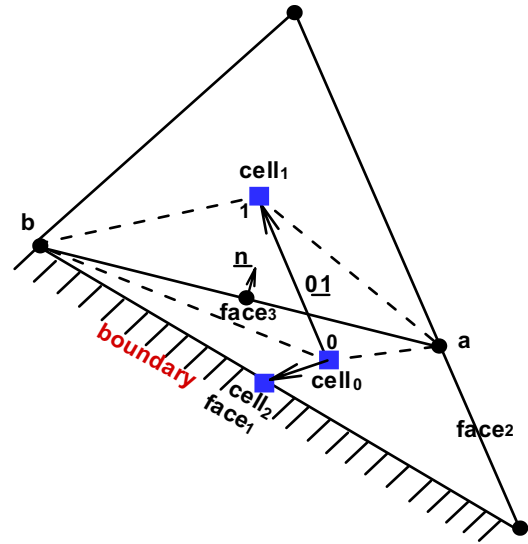$$

Fig. 1. Diagram of the unstructured finite volume and notations.

where J_f is the mass flow rate which is defined to be positive for the flow leaving Ω_0 and will be addressed in the later section. D_f represents the diffusion transport through the face "$face_f$". The summations are over the faces of the control volume.

2.5. Convection flux: $J_f\Phi_f$

The mass flow rate J_f at the face "$face_f$" is determined when solving the momentum and the continuity equations. The convective flux can then be determined upon evaluating the face value of Φ_f. In the absence of a line structure, the values of the variable and its derivatives cannot be written in terms of cell values using a one-dimensional Taylor series expansion. To overcome this difficulty, several gradient reconstruction strategies are proposed [23–25]. Among them, the CVFEM method [24] employs the shape function and another approach uses the least squares technique [23]. However, these techniques can be quite expensive and are dependent on the cell-shape. If a shape-independent formulation [5] for the cell gradients can be devised using the divergence theorem, a hyper-order accurate value of Φ_f at the cell face could be obtained by using the following formula:

$$
\Phi_f = \Phi_{\text{upwind}}^{n+1} + \underline{\nabla}\Phi_{\text{upwind},r}^n \cdot d\underline{r}, \tag{15}
$$

where $d\underline{r}$ is the vector that directs from the centroid of an upwind cell to the center of the face, $\Phi_{\text{upwind}}^{n+1}$ is the value from an upwind cell and the reconstructed gradient $\underline{\nabla}\Phi_{\text{upwind},r}^n$ is evaluated from the upwind cell at the time instant t_n. Note that the value itself is treated implicitly while the gradient is evaluated explicitly. The implementation of this upwind reconstruction has been addressed in Appendix A.

2.6. Diffusion flux: D_f

For the non-moving grid system, the time derivative term on the left-hand side of Eq. (13) can be placed outside of the volume integral. It should be noted that the diffusion

term at the face, as defined in Eq. (6), is derived from the Gauss divergence theorem

$$D_f \equiv \Gamma \langle \underline{\nabla} \Phi \rangle_f \cdot \underline{A}_f, \tag{16}$$

Γ is the transport coefficient such as the viscosity in the momentum equations. In Eq. (16), $\langle \underline{\nabla} \Phi \rangle_f \cdot \underline{A}_f$ is discretized in a manner similar to the Crank–Nicolson method frequently used in the predication of time dependent diffusion equation

$$\langle \underline{\nabla} \Phi \rangle_f \cdot \underline{A}_f = \underbrace{(\Phi_1 - \Phi_0) \left(\frac{\underline{A}_f \cdot \underline{A}_f}{\underline{A}_f \cdot \underline{01}} \right)}_{\text{First term}}$$

$$+ \underbrace{\langle \overline{\underline{\nabla} \Phi} \rangle \cdot \left(\underline{A}_f - \underline{01} \frac{\underline{A}_f \cdot \underline{A}_f}{\underline{A}_f \cdot \underline{01}} \right)}_{\text{Second term}}$$

$$\approx \frac{1}{2} \left[(\Phi_1 - \Phi_0)^{n+1} + (\Phi_1 - \Phi_0)^n \right] \left(\frac{\underline{A}_f \cdot \underline{A}_f}{\underline{A}_f \cdot \underline{01}} \right)$$

$$+ \langle \overline{\underline{\nabla} \Phi} \rangle_f^n \cdot \left(\underline{A}_f - \underline{01} \frac{\underline{A}_f \cdot \underline{A}_f}{\underline{A}_f \cdot \underline{01}} \right). \tag{17}$$

A detail derivation of Eq. (17) is given in Appendix A. At a $face_f$, $\langle \overline{\underline{\nabla} \Phi} \rangle_f^n$ is taken to be the averaged derivative determined from the values calculated at the two adjacent cells. The volume averaged property $\langle \underline{\nabla} \Phi \rangle_0$ is evaluated using the Gauss divergence theorem and will also be addressed in Appendix A. There are several methods, addressed in a detailed manner in [23–25], for evaluating gradients. In the present study, a cell-center based gradient reconstruction [5] is adopted due to its simplicity and minimal computational effort. The face vector $\underline{A}_f$ is outward and normal to the $face_f$ for the cell Ω_0 and $\underline{01}$ is the position vector from the center of Ω_0 to the center of Ω_1, which is the neighbor cell of Ω_0. The first term in Eq. (17) is of the first-order accuracy in space and the second term is a hyper-order (super-linear) correction. It has been addressed in [28–30] that the second-order accuracy in space could be achieved if the cell is orthogonal and quadrilateral. The boundary diffusion flux can then be treated in the same manner as that for an interior face. The flux D_2 at a boundary, see Fig. 1, can be written as

$$D_2 \equiv \Gamma \langle \underline{\nabla} \Phi \rangle_f \cdot \underline{A}_f$$

$$\approx \frac{\Gamma}{2} \left[(\Phi_2 - \Phi_0)^{n+1} + (\Phi_2 - \Phi_0)^n \right] \frac{\underline{A}_f \cdot \underline{A}_f}{\underline{A}_f \cdot \underline{02}}$$

$$+ \left[\Gamma \langle \overline{\underline{\nabla} \Phi} \rangle_f^n \cdot \left(\underline{A}_f - \underline{02} \frac{\underline{A}_f \cdot \underline{A}_f}{\underline{A}_f \cdot \underline{02}} \right) \right]^n, \tag{18}$$

where Φ_2 is the value at the center of the boundary face and $\underline{02}$ is the vector from the center of the cell Ω_0 to the centroid of boundary face. For the Neumann boundary conditions, the specified flux can be directly added to the control volume balance. Eq. (18) is also employed to compute the boundary values.

2.7. Discretization of momentum equation

In a similar manner, the momentum equation is discretized as the general scalar equation described above. The source term contains the pressure gradient and the components of the stress tensor are not included in the standard diffusion term:

$$\frac{\partial}{\partial x_j} \left(\mu \frac{\partial u_j}{\partial x_i} - \frac{2}{3} \delta_{ij} \mu \frac{\partial u_l}{\partial x_l} - \delta_{ij} P \right). \tag{19}$$

Eq. (19) is discretized and integrated over the control volume Ω_0, resulting in the following equation:

$$\sum_f \left(\mu_f \frac{\partial u_j}{\partial x_i} - \frac{2}{3} \delta_{ij} \mu_f \frac{\partial u_l}{\partial x_l} - \delta_{ij} P_f \right)^n A_j, \tag{20}$$

where the viscosity μ_f, the extra shear, and pressure forces at the cell face are evaluated by averaging the cell derivatives and cell values, respectively.

2.8. Mass flow rate J_f

Since the pressure and the velocity components are stored at the cell centers, the evaluation of the mass flow rate at a cell face J_f by averaging the cell center velocities
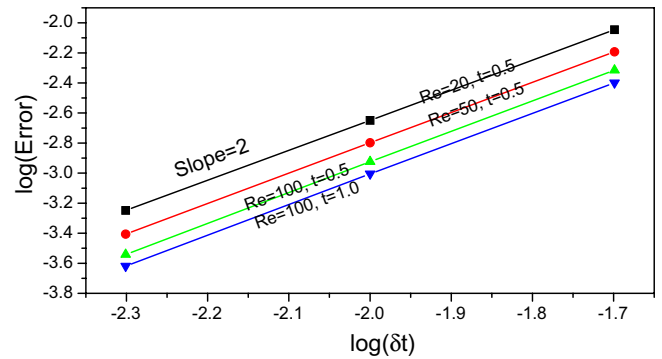

Fig. 2. The predicated maximum error in u (x-component velocity) for showing that the temporal rate of convergence is second-order accuracy.
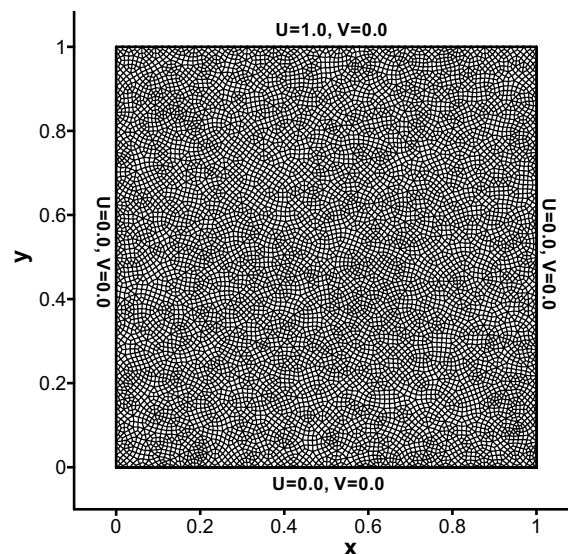

Fig. 3. Mesh and boundary conditions for the driven cavity flow.

is prone to wavy modes and checker-board pressure patterns. To overcome this drawback, a scheme [20,27] similar to that of Rhie and Chow [2] is used. For the face "$face_f$"

in Fig. 1, the mass flow rate J_f^n used in momentum equations to advance time step is derived from Eq. (10) and is determined by virtue of the following equation:
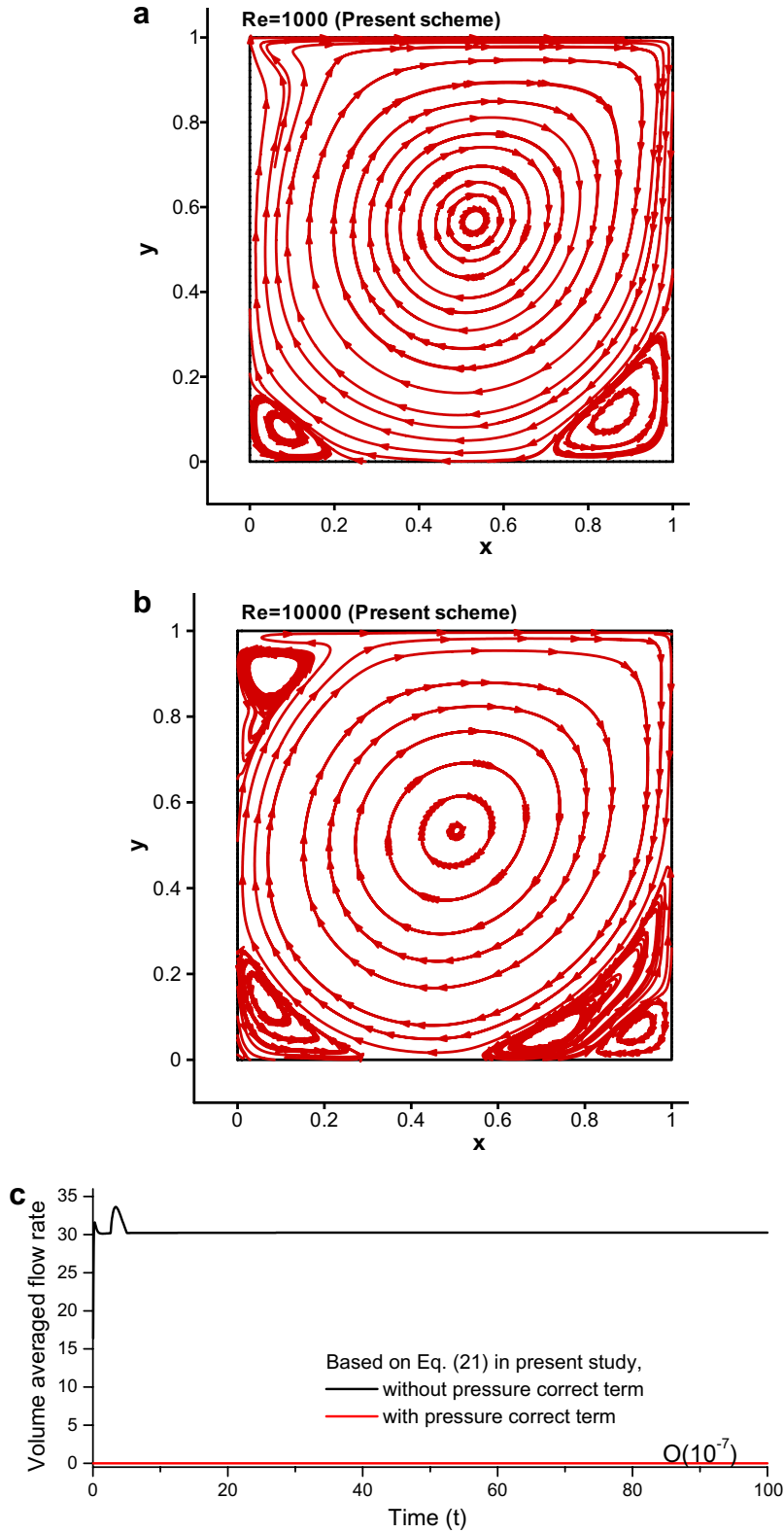

Fig. 4. Present scheme for streamline plot for the driven cavity flow: (a) $Re = 1000$, (b) $Re = 10,000$, (c) plot of the maximum volume averaged flow rate against time at $Re = 1000$.

$$\frac{\rho(\underline{U}_f - \underline{U}_f^*) \cdot \underline{A}_f}{\delta t} = -\langle \underline{\nabla} P \rangle_f \cdot \underline{A}_f \Rightarrow J_f \equiv \rho \underline{U}_f \cdot \underline{A}_f$$

$$= \underbrace{\rho \left(\frac{\underline{U}_0^* + \underline{U}_1^*}{2} \right) \cdot \underline{A}_f}_{\rho \underline{U}_f^*} - (\delta t)\langle \underline{\nabla} P \rangle_f \cdot \underline{A}_f \Rightarrow J_f^n$$

$$= \rho \left(\frac{\underline{U}_0^n + \underline{U}_1^n}{2} \right) \cdot \underline{A}_f$$

$$- \underbrace{(\delta t)\left[((P_1^n - P_0^n) - \langle \overline{\nabla P} \rangle_f^n \cdot \underline{01}) \frac{\underline{A}_f \cdot \underline{A}_f}{\underline{A}_f \cdot \underline{01}} \right]}_{\text{pressure correction term}},$$

$$(21)$$

where $\underline{U}_0^*$ is the intermediate velocity defined in Eq. (10) and is located at the center of cell Ω_0. $\langle \underline{\nabla} P \rangle_f \cdot \underline{A}_f$ is determined using the similar procedure as Eq. (17). After a simple operation, the Rhie and Chow pressure correction term is shown in Eq. (21). $\langle \overline{\nabla P} \rangle_f$ is the averaged pressure gradient from the adjacent two cells. It is important to note that the face velocity is obtained from Eq. (21) rather than from the interpolated adjacent cell-center velocities. The divergence-free velocity field $\underline{U}_f^n$ is used for the calculation of the convective fluxes in momentum equations for advancing time step. This procedure ensures strong coupling between the pressure and the velocity. A similar
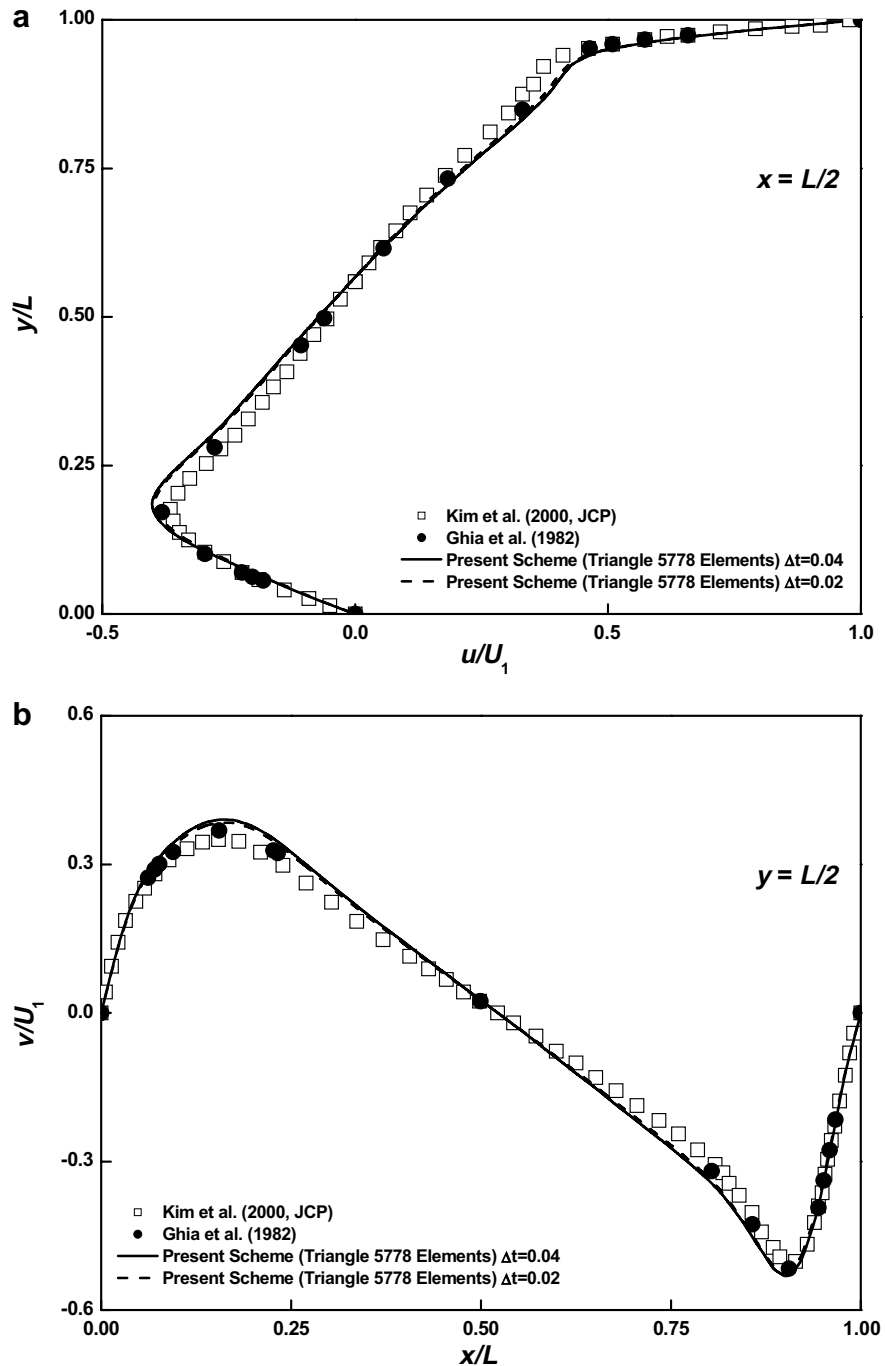

Fig. 5. The simulated velocity profiles at different time step sizes: (a) u-velocity, (b) v-velocity ($Re = 1000$, 6778 triangles).

procedure of using the momentum interpolation method can be found in Zang et al. [3] for the structured grids in curvilinear coordinates. Those schemes have been successfully applied to a variety of incompressible flow problems. An implicit method is preferred when the time step limitation imposed by an explicit or semi-implicit stability bound is significantly less than that imposed by the accuracy requirement. If the flow geometry contains sharp corners which exist in many flow geometries, rapid variation of

flow variables in their vicinity would require dense grid clustering which restricts the computational time step. A fully implicit method overcomes this restriction with a trade-off of possible higher operation counts per time step. For example, Choi et al. [26] used a fully implicit method in a curvilinear coordinate system to simulate the flow over ribs. The required CPU time can be reduced much as compared to that using a conventional semi-implicit method.
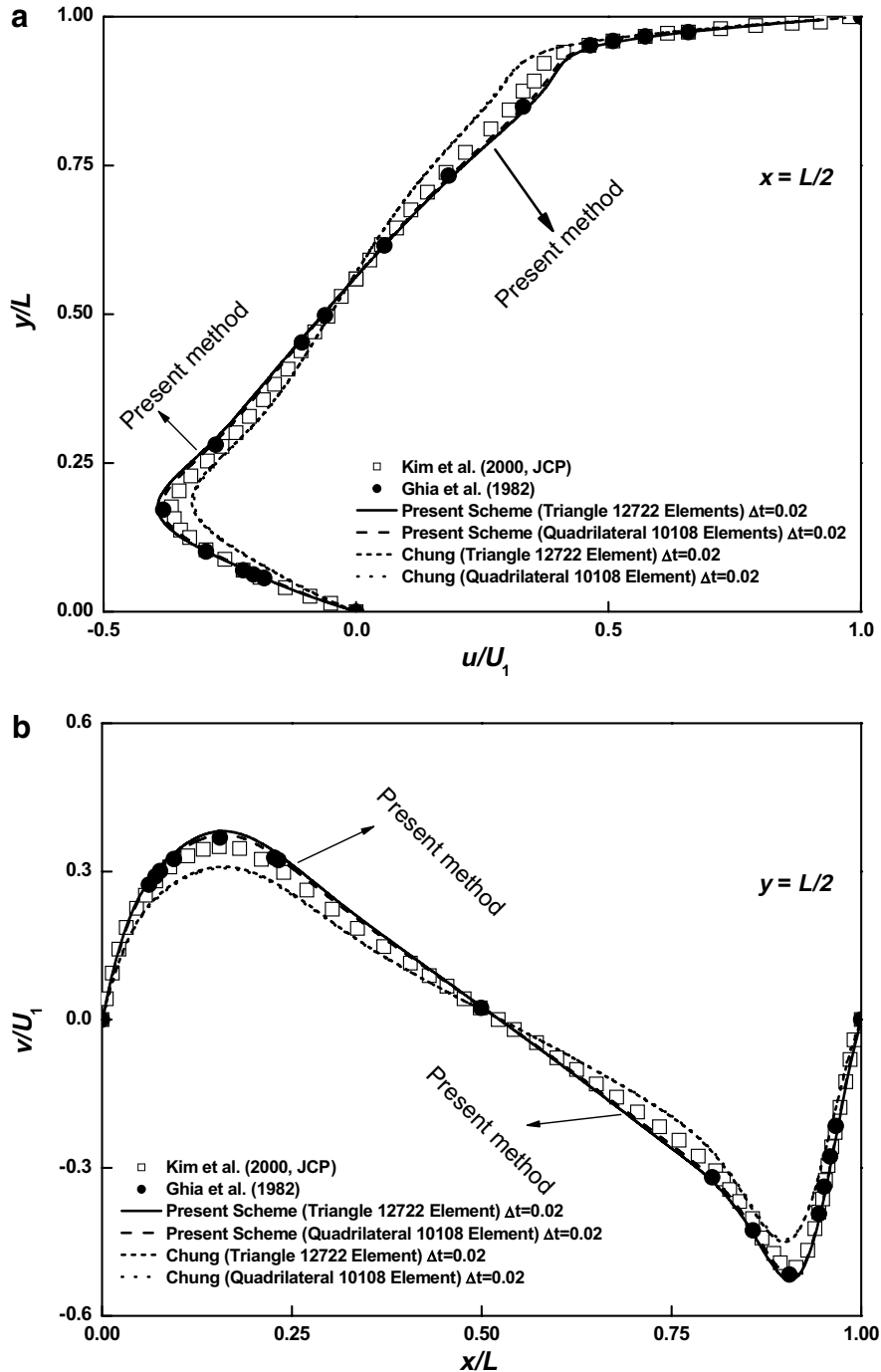

Fig. 6. The simulated velocity profiles at different time step sizes: (a) u-velocity, (b) v-velocity ($Re = 1000$, 12,722 triangles and 10,108 quadrilaterals).

2.9. Pressure equation

In an operator splitting method the pressure equation shown in Eq. (22) is constrained by the assumption of incompressible fluid flow. It results in

$$\underline{\nabla}^2 P^{n+1} = \frac{1}{\delta t} \underline{\nabla} \cdot (\rho \underline{U}^*). \tag{22}$$

After discretization and integration of Eq. (22) over the control volume Ω_0, the following equation is obtained:

$$A_0 P_0^{n+1} + \sum_{nb} A_{nb} P_{nb}^{n+1} = -\frac{1}{\delta t} \sum (\rho \underline{U}^* \cdot \underline{A})_f$$
$$+ \sum_f \left[\langle \underline{\nabla P} \rangle_f^n \cdot \left(\underline{A}_f - \underline{01} \frac{\underline{A}_f \cdot \underline{A}_f}{\underline{A}_f \cdot \underline{01}} \right) \right],$$

$$A_{nb} = -\frac{\underline{A}_f \cdot \underline{A}_f}{\underline{01} \cdot \underline{A}_f}, \quad A_0 = -\sum_{nb} A_{nb}. \tag{23}$$
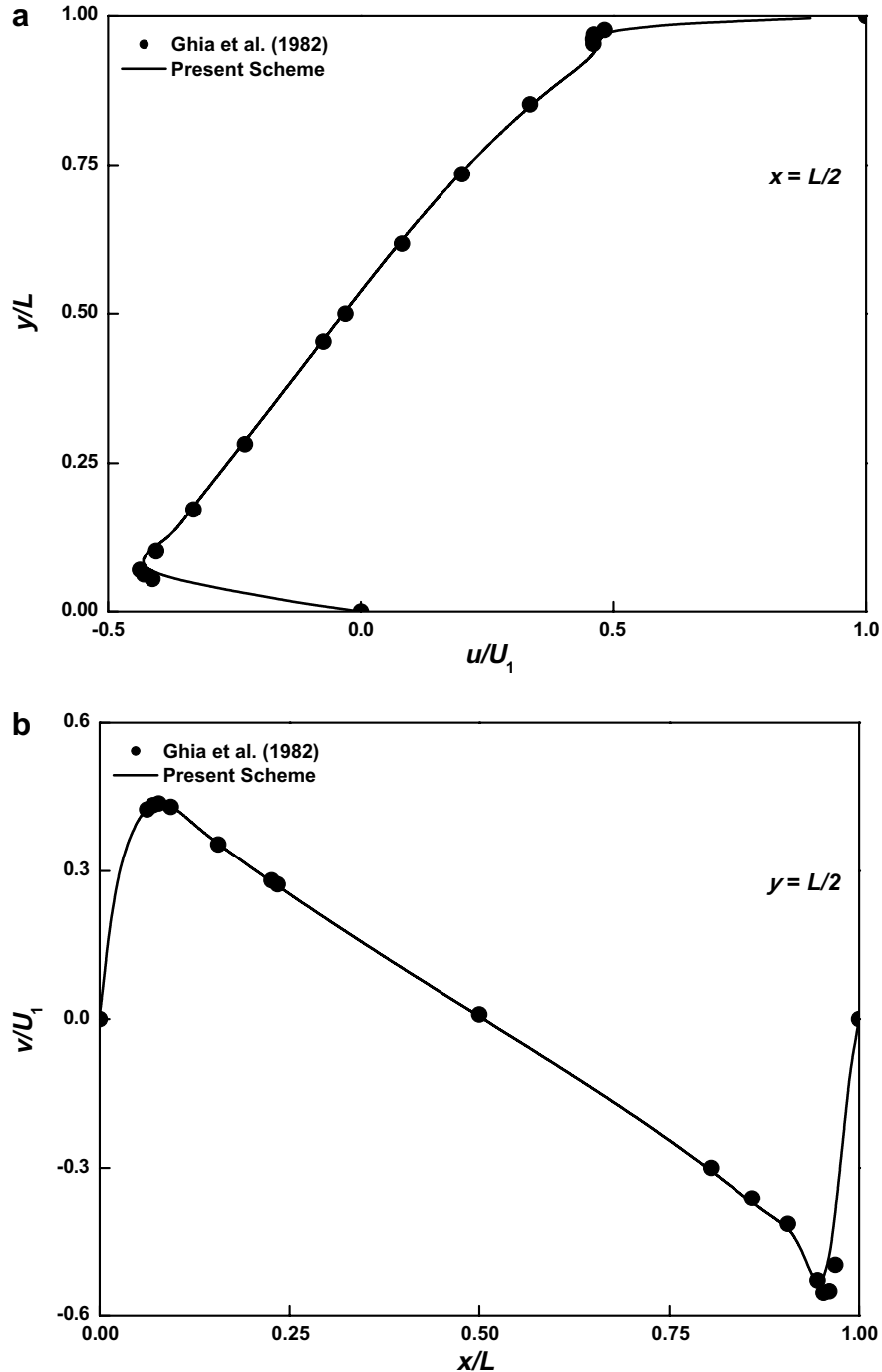

Fig. 7. Comparison of the simulated velocity profiles: (a) u-velocity, (b) v-velocity ($Re = 5000$).

Once the solution of Eq. (23) is obtained through the pre-conditioned CG solver, the velocity and pressure fields are updated using Eq. (10). If the pressure on a boundary is not known prior, however, knowing the velocity, a Neumann type of boundary condition, Eq. (10) is employed.

2.10. Equation solver

The number of neighboring cells in Eq. (10) or Eq. (14) could be arbitrary for an unstructured grid. Ss a conse-quence, the familiar line-by-line iterative solvers cannot be used. Instead, the system is solved using a pre-conditioned conjugate gradient method. Two algorithms of the conju-gate gradient (CG) method [22] are used in the present study. The P-CG method is used for the pressure correction equation since it gives rise to a symmetric and positive def-inite coefficient matrix. The P-BiCGSTAB method [22] is selected for the momentum equation. The convergence cri-terion is that the normalized residuals given below over all the cells are less than our prescribed value, usually 10^{-6}
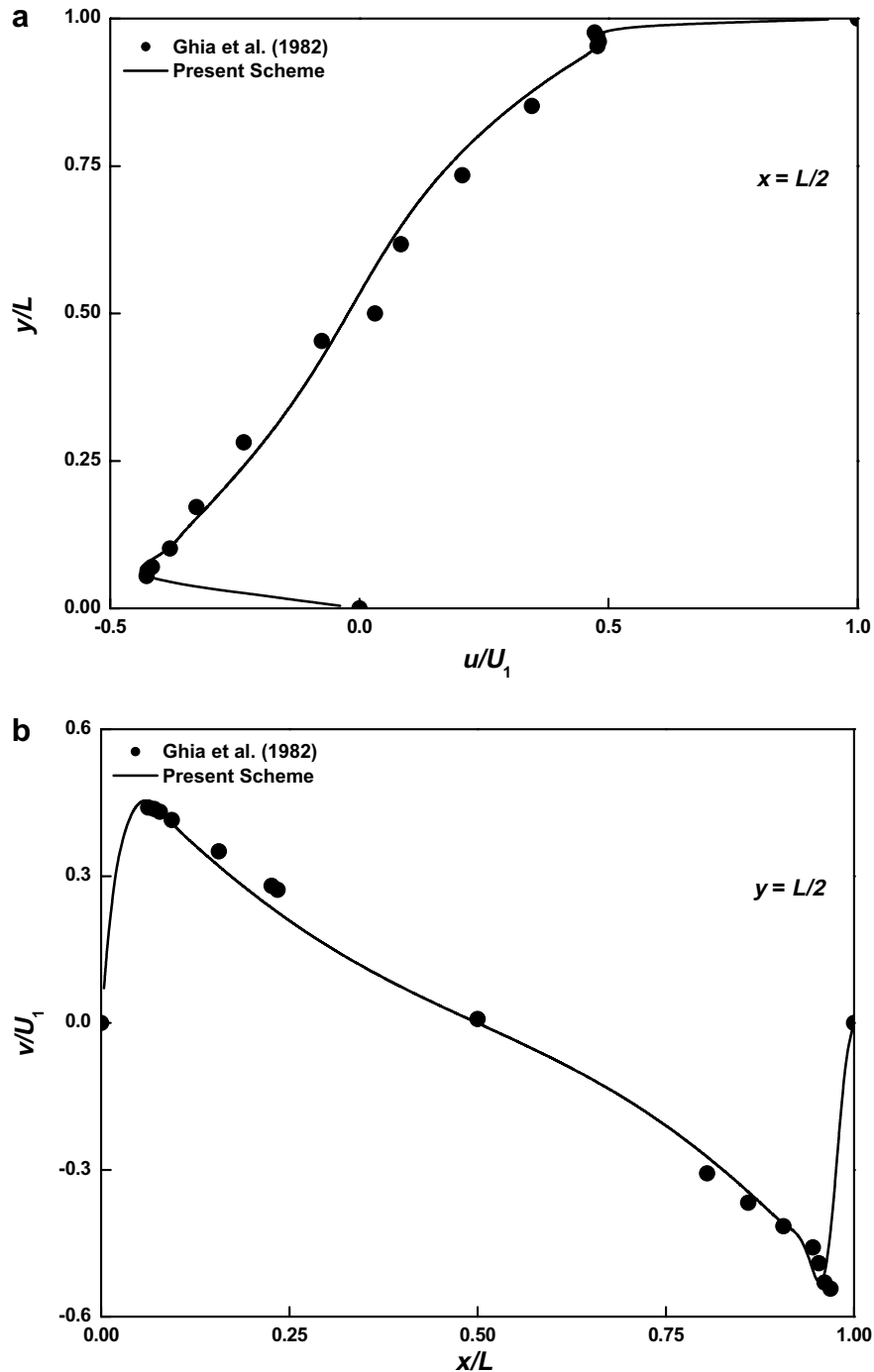

Fig. 8. Comparison of the simulated velocity profiles: (a) u-velocity, (b) v-velocity ($Re = 10{,}000$).

$$\begin{cases} \underline{R} \equiv \underline{A}\underline{\Phi} - \underline{B}; & \underline{R} = (R_1, R_2, \ldots, R_c, \ldots, R_{\text{Mcell}}), \\ \underbrace{\dfrac{\|R_c\|}{\|\Omega_c\|}}_{\text{normalized residual}} < 10^{-6}, & c = 1, 2, \ldots, \text{Mcell}. \end{cases} \quad (24)$$

In the above, $\underline{A}$ is the system equations and vector $\underline{B}$ is the assembled term from the time dependent convection, and diffusion with proper boundary conditions specified.

"Mcell" is the number of cells in the domain. $\|\Omega_c\|$ is the volume of Ω_c.

3. Numerical examples

Example 1 (*Decaying Vortex*). The temporal accuracy of the present numerical method is verified by simulating the following two-dimensional unsteady flow, which has been investigated by the previous researchers [1,3,20]:
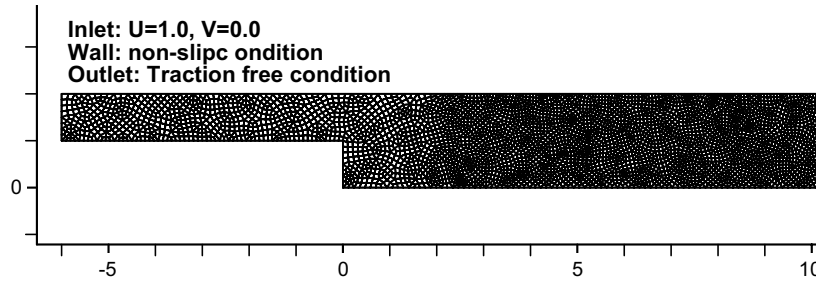

Fig. 9. Mesh and associated boundary conditions for the backward-facing step problem.
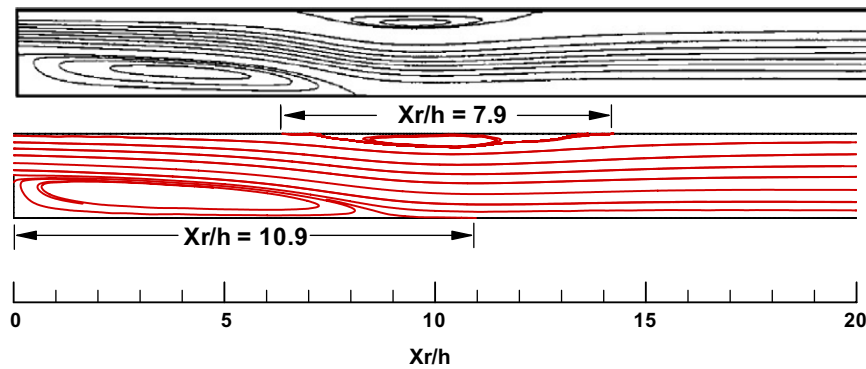

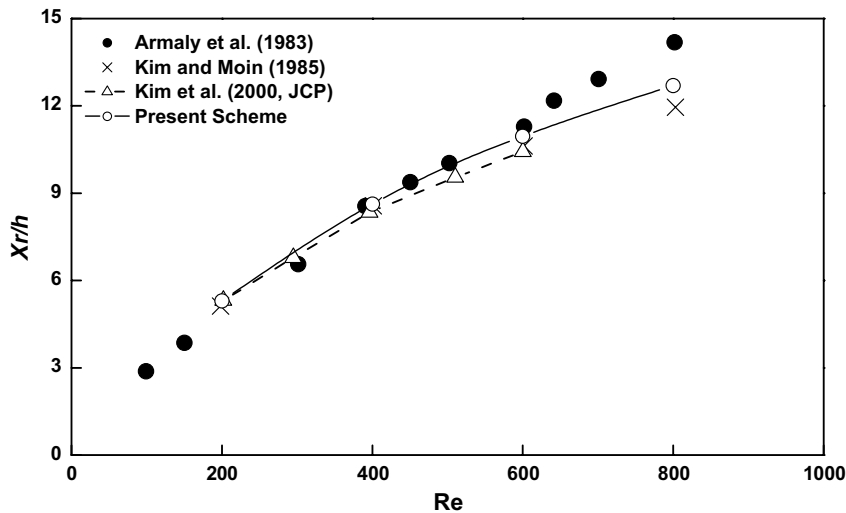Fig. 10. Comparison streamlines near the backward-facing step ($Re = 600$).

Fig. 11. Plot of the reattachment length against the Reynolds number.

$$u(x,y,z) = -[\cos(\pi x)\sin(\pi y)]e^{-2\pi^2 t/Re},$$
$$v(x,y,z) = -[\sin(\pi x)\cos(\pi y)]e^{-2\pi^2 t/Re}, \qquad (25)$$
$$p(x,y,z) = -\frac{1}{4}\left[\cos(2\pi x) + \cos(2\pi y)\right]e^{-4\pi^2 t/Re}.$$

The computational domain is $-1/2 \leqslant x, y \leqslant 1/2$ and the computations are carried out at $Re = 20$–100, where $Re = U_{max}L/v$, and U_{max} is the initial maximum velocity and $L = 1$ is the size of a vortex. The initial velocity condition at $t = 0$ and the velocities at the time-varying boundaries are provided from the exact solution. The temporal accuracy is investigated by varying the time step but keeping the mesh size fixed. Here, the orthogonal grids of 100×100 cells are used to minimize the spatial error. The current operator splitting method is verified to have the second-order time accuracy as shown in Fig. 2.

Example 2 (*Lid-Driven Cavity Flow*). The geometry, boundary conditions, and grid for the flow in a lid-driven square cavity [15,20,21] are shown in Fig. 3. The Reynolds number is defined as $Re = U_s L/v$, where $U_s = 1$ is the velocity of the top lid and $L = 1$ is the length of the bottom wall. A calculation is performed at $Re = 1000$ and $Re = 10,000$ with an unstructured grid shown in Fig. 4a and b. In this calculation, the maximum CFL number is around 3.5. In order to illustrate the effect of pressure correction term in Eq. (21), the absolute maximum error is against time in Fig. 4c. Figs. 5–8 shows the centerline velocities $u(x)$ and $v(y)$ along the vertical and horizontal centerlines, respectively. It is noted that the results using the present scheme is independent of the time step size used as shown in Fig. 5. In addition, to get the mesh independent solution, different types mesh such as triangle and quadrilateral are used and the results are shown in Fig. 6. It is also clear that the present results are shown to have an excellent agreement with the data from Ghia et al.

[15]. However, the results from Chung are suppressed; in other words, it introduces much upwind effect in his implicit scheme. Flows of $Re = 5000$ and $Re = 10,000$ are tested further and the results are compared well with the Ghia et al. [15], as shown in Figs. 7 and 8.
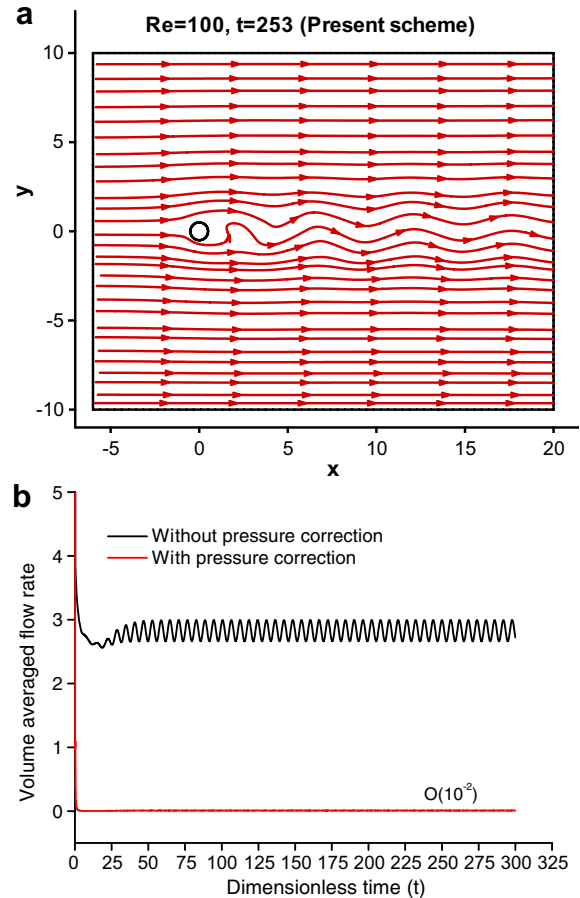

Fig. 13. (a) Plot of the streamlines for flow over a circular cylinder. (b) Plot of the maximum volume averaged flow rate against time at $Re = 100$.
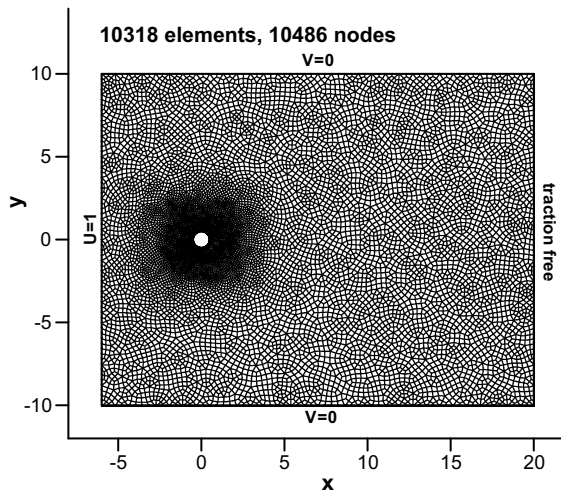

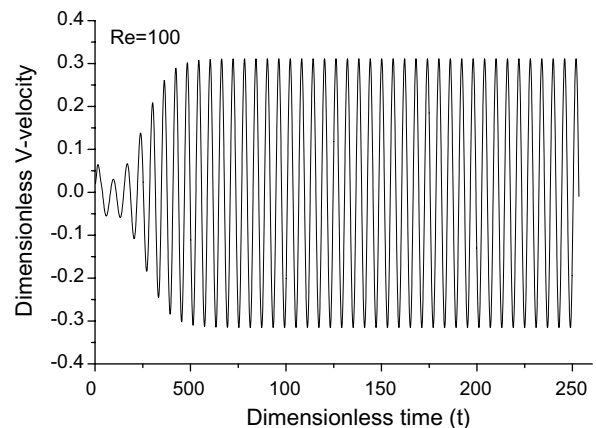Fig. 12. Mesh and boundary conditions for the flow over a circular cylinder.

Fig. 14. Plot of flow induced y-direction velocity.

Example 3 (*Backward-Facing Step Flow*). Another widely used benchmark problem to examine the accuracy of the numerical method is the backward-facing step in a channel flow. The flow geometry and boundary conditions are described in Fig. 9. The expansion ratio is 1:2 and the length of the computational domain is $30h$, where h is the step height. The uniform flow at the entrance is specified and the traction free boundary condition [21] is specified at the outlet to obtain the pressure, $P_f^{n+1} = \mu(\underline{n})^t \cdot \underline{\tau}_f^n \cdot (\underline{n})$. $\underline{\tau}$ is defined in Eq. (1). To solve $\widehat{U}$ in the momentum equation, $(\partial \underline{U} / \partial n)^n = 0$ is specified at the outlet and this specification is also applied in Example 4. An unstructured grid of 8831 quadrilateral is used as shown in Fig. 9. Calculations are performed at $Re = 200, 400$, and $Re = 600$, where $Re = U_b 2h/v$ and U_b is the bulk velocity. The computational time step is fixed to satisfy the maximum CFL around 2–3. Fig. 10 shows the calculated reattachment length as a function of the Reynolds number, in compari-

son with the previous results of Armaly et al. [16], Kim and Moin [1] and Kim and Choi [20]. The present result is in good agreement with the computational result of Kim and Moin [1] and Kim and Choi [20] for all the investigated Reynolds numbers calculated. However, at $Re > 400$, a difference exists between the computational (present study and [1]) and the experimental results [16]. This difference may result from the three-dimensionality of the flow as Armaly et al. [16] pointed out. At $Re = 600$, a secondary separation recirculation length exists on the upper wall (Figs. 10 and 11). The length is $7.9h$, which agrees well $7.8h$ which was obtained from Kim and Moin [1].

Example 4 (*Flow over a Circular Cylinder*). Flow over a circular cylinder at $Re > 47$ is a typical example of unsteady flow because vortex shedding takes place at that Reynolds number range [17,18]. Fig. 12 shows the geometry and
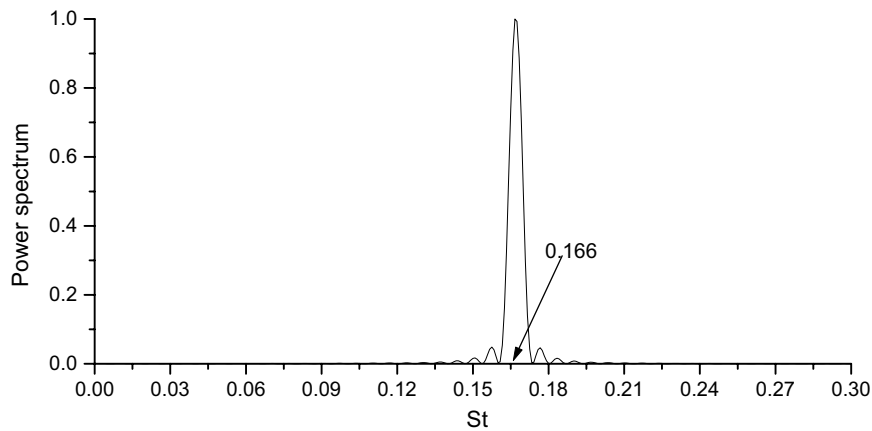

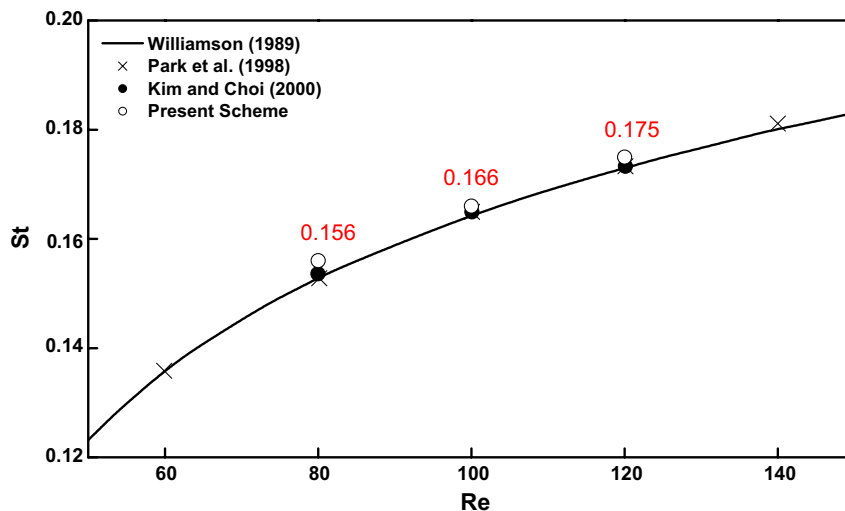Fig. 15. Plot of spectrum for the flow over a circular cylinder at $Re = 100$.

Fig. 16. Plot of the Strouhal number against the Reynolds number (Williamson [19]: $St = -3.3265/Re + 0.1816 + 1.6 \times 10^{-4} Re$).

boundary conditions for the flow. The computational domain is $-6d \leqslant x \leqslant 20d$ and $-10d \leqslant y \leqslant 10d$, where d is the diameter of the cylinder and ($x = 0$; $y = 0$) corresponds to the center of the cylinder. Again, the traction free boundary condition is specified at the outlet.

Fig. 12 shows an unstructured grid with 10318 quadrilaterals used in this study. Calculations are performed at three different Reynolds numbers: $Re = 80$, 100, and $Re = 120$, where $Re = u_b L/v$ and u_b is the uniform inlet velocity. The computational time step is fixed to satisfy the maximum CFL which is around 2–3. Fig. 13a shows the streamline pattern to demonstrate the induced vortex shedding at $t = 253$. In order to illustrate the effect of pressure correction term in Eq. (21), the absolute maximum error is against time in Fig. 13b. Fig. 14 shows the time varying $v(y)$ velocity. The spectrum results show that the Strouhal number is 0.166 at the Reynolds number 100, as shown in Fig. 15. The Strouhal number is a function of Reynolds number, where $St = fd/u_b$ and f is the shedding frequency. The calculated Strouhal number is compared with the experimental correlation of Williamson's [19] and the computational result of Park et al. [17] shown in Fig. 16. An excellent agreement is found among these results.

4. Conclusions

The present numerical method is applied to four benchmark problems and the results show good agreement with the previous experimental and numerical results. Consequently, the following conclusions are drawn from the above simulation results:

1. A quasi-implicit fractional-step method is presented for evaluating the unsteady incompressible flow on unstructured grids.
2. A non-staggered grid system is employed rather than a staggered grid system because of the simplicity and ease of extension to three dimensions. Convection is suppressed for those cells with all nodes located at the wall in both finite volume and finite element methods. This convection is retained when using the cell-centered finite volume method.
3. In this study, the momentum interpolation method, developed by Rhie and Chow [2] and was further extended by Zang et al. [3], is applied to problems with unstructured grids to eliminate the wavy mode and the checker-board pressure pattern occurring in a non-staggered grid system.
4. In order to remove the time step restriction and to reduce the required CPU time for complex geometries, a fully implicit time-advancement scheme is used. The nonlinear equations resulting from this fully implicit scheme are linearized without losing the overall time accuracy. Based on the proposed modified implicit scheme, the second-order time accuracy has been briefly

demonstrated from the one-dimensional point of view and is validated by the two-dimensional decaying vortice, as illustrated in Example 1.
5. The system matrices are solved using the P-BiCGSTAB for the momentum equations and the P-CG method is used to solve the pressure equation so as to update the velocity.

Appendix A. $(\underline{\nabla}\phi)_f \cdot \underline{A}_f$

As shown in Fig. 1, both geometry configuration and definition are specified. For the two-dimensional gradient flux, the face vector is expressed as $\underline{A}_f = \underline{ab} \times \underline{k}$. $\underline{k}$ is the third directional unit vector normal to vectors $\underline{ab}$ and $\underline{01}$. By introducing the local base vector, the gradient based on a cell can be expressed as

$$\underline{\nabla}\phi = \underline{g}^1 \frac{\partial \phi}{\partial x^1} + \underline{g}^2 \frac{\partial \phi}{\partial x^2}, \qquad (A1)$$

x^1 is the coordinate along the vector $\underline{ba}$ and x^2 is the second coordinate along $\underline{01}$. Here, the local base vectors $\underline{g}_1$ and $\underline{g}_2$ are defined as $\underline{g}_1 \equiv \underline{ba}/|\underline{ba}|$ and $\underline{g}_2 \equiv \underline{01}/|\underline{01}|$, respectively. The length of a vector $\underline{ba}$ is defined as $|\underline{ba}|$. In this study, the particular domain is restricted to Ω_f, which is the domain confined by the dash line as shown in Fig. 1. With the above definitions, Eq. (A1) is integrated over Ω_f to result in

$$\langle\underline{\nabla}\phi\rangle_{\Omega_f} = \langle\underline{g}^1\rangle\left\langle\frac{\partial \phi}{\partial x^1}\right\rangle + \langle\underline{g}^2\rangle\left\langle\frac{\partial \phi}{\partial x^2}\right\rangle$$
$$= \langle\underline{g}^1\rangle\frac{\phi_a - \phi_b}{|\underline{ba}|} + \langle\underline{g}^2\rangle\frac{\phi_1 - \phi_0}{|\underline{01}|}. \qquad (A2)$$

The notation of $\langle\underline{\nabla}\phi\rangle_{\Omega_f}$ is denoted as the operation of $\langle\underline{\nabla}\phi\rangle_{\Omega_f} \equiv \int_{\Omega_f}\underline{\nabla}\phi \, \mathrm{d}\Omega/\Omega_f$. The local reciprocal base vectors, $\langle g^1\rangle_{\Omega_f}$ and $\langle g^2\rangle_{\Omega_f}$, are therefore expressed by the following two equations:

$$\langle\underline{g}^1\rangle_{\Omega_f} = \frac{|\underline{ba}|}{\underline{k} \cdot (\underline{ba} \times \underline{01})}(\underline{01} \times \underline{k}), \qquad (A3)$$

$$\langle\underline{g}^2\rangle_{\Omega_f} = \frac{|\underline{01}|}{\underline{k} \cdot (\underline{ba} \times \underline{01})}(\underline{k} \times \underline{ba}). \qquad (A4)$$

Upon substituting the $\langle g^1\rangle_{\Omega_f}$ and $\langle g^2\rangle_{\Omega_f}$ into Eq. (A2), we have the equation as follows:

$$\langle\underline{\nabla}\phi\rangle_{\Omega_f} = \frac{\underline{k} \times \underline{ba}}{\underline{k} \cdot (\underline{ba} \times \underline{01})}(\phi_1 - \phi_0) + \frac{\underline{01} \times \underline{k}}{\underline{k} \cdot (\underline{ba} \times \underline{01})}(\phi_a - \phi_b).$$
$$(A5)$$

The value of $\langle \underline{\nabla}\phi \rangle_{\Omega_f}$ can be regarded as the gradient at the $face_f$ in practice. Thus, $\langle \underline{\nabla}\phi \rangle_{\Omega_f} \approx (\underline{\nabla}\phi)_f$ is assumed if the volume of Ω_f is limited to a very small scale. Through the mean value theorem, we can easily obtain the result of $(\underline{\nabla}\phi)_f \cdot \underline{A}_f$ and the result is expressed below

$$(\underline{\nabla}\phi)_f \cdot \underline{A}_f \approx \langle \underline{\nabla}\phi \rangle_{\Omega_f} \cdot (\underline{ab} \times \underline{k})$$

$$= \frac{\underline{A}_f \cdot \underline{A}_f}{\underline{k} \cdot (\underline{ba} \times \underline{01})}(\phi_1 - \phi_0) + \frac{\underline{01} \cdot \underline{ab}}{\underline{k} \cdot (\underline{ba} \times \underline{01})}$$
$$\times (\phi_a - \phi_b). \tag{A6}$$

It is also noted that $\underline{k} \cdot (\underline{ba} \times \underline{01})$ is equivalent to $\underline{01} \cdot \underline{A}_f$. Further simplification of Eq. (A6) yields

$$(\underline{\nabla}\phi)_f \cdot \underline{A}_f \approx \frac{\underline{A}_f \cdot \underline{A}_f}{\underline{01} \cdot \underline{A}_f}(\phi_1 - \phi_0) + \frac{\underline{01} \cdot \underline{ab}}{\underline{01} \cdot \underline{A}_f}(\phi_a - \phi_b). \tag{A7}$$

The first term in the right-hand side of Eq. (A7) represents the primary gradient. The second term in the right hand side of Eq. (A7) is the secondary or cross-diffusion term and is zero when $\underline{ba} \cdot \underline{A}_f = 0$. An alternative but efficient formula recommended by [8] is defined as Eq. (A8) to treat the second term in Eq. (A7).

$$(\underline{\nabla}\phi)_f \cdot \underline{A}_f \approx \frac{\underline{A}_f \cdot \underline{A}_f}{\underline{A}_f \cdot \underline{01}}(\phi_1 - \phi_0)$$
$$+ \left[\overline{\underline{\nabla}\phi} \cdot \left(\underline{A}_f - \underline{01}\frac{\underline{A}_f \cdot \underline{A}_f}{\underline{A}_f \cdot \underline{01}} \right) \right]. \tag{A8}$$

The smooth gradient $(\overline{\underline{\nabla}\phi})_f$ is defined as $(\overline{\underline{\nabla}\phi})_f = 0.5((\overline{\underline{\nabla}\phi})_0 + (\overline{\underline{\nabla}\phi})_1)$, where $(\overline{\underline{\nabla}\phi})_0$ is obtained through the following steps.

(1) The reconstruction gradient $\underline{\nabla}\phi_{r,0}$ is estimated as shown in Eq. (A9).

$$\underline{\nabla}\phi_{r,0} = \frac{1}{\Omega_0}\sum_f \phi_f \underline{A}_f, \tag{A9}$$

where the summation is over all the faces of $cell_0$. The face value of ϕ is obtained by averaging the values at the neighboring cells and is defined as

$$\phi_f = \frac{\phi_0 + \phi_1}{2}. \tag{A10}$$

(2) The smooth gradient of ϕ for $cell_0$ can be evaluated by

$$(\overline{\underline{\nabla}\phi})_0 = \frac{1}{\Omega_0}\sum_f \overline{\phi}_f \underline{A}_f. \tag{A11}$$

Eq. (A12) enable us to obtain the expression of $\overline{\phi}_f$.

$$\overline{\phi}_f = \frac{\phi_{f,0} + \phi_{f,1}}{2}. \tag{A12}$$

Using the reconstruction gradient $\underline{\nabla}\phi_{r,0}$, the value $\phi_{f,0}$ at the face of $cell_0$ can be defined as

$$\phi_{f,0} = \phi_0 + (\underline{\nabla}\phi)_{r,0} \cdot \underline{0f}, \tag{A13}$$

where $\underline{0f}$ is denoted as the displacement vector from the center of $cell_0$ to the associated center of $face_f$.

References

[1] J. Kim, P. Moin, Application of a fractional-step method to incompressible Navier–Stokes equations, J. Comput. Phys. 59 (1985) 308–323.

[2] C.M. Rhie, W.L. Chow, Numerical study of the turbulent flow past an airfoil with trailing edge separation, AIAA J. 21 (1983) 1525–1532.

[3] Y. Zang, R.L. Street, J.R. Koseff, A non-staggered grid, fractional step method for time-dependent incompressible Navier–Stokes equations in curvilinear coordinates, J. Comput. Phys. 114 (1994) 18–33.

[4] L. Davidson, A pressure correction method for unstructured meshes with arbitrary control volumes, Int. J. Numer. Methods Fluids 22 (1996) 181–265.

[5] S.R. Mathur, J.Y. Murthy, A pressure-based method for unstructured meshes, Numer. Heat Transfer Part B 31 (1997) 195–215.

[6] Y.G. Lai, An unstructured grid method for a pressure-based flow and heat transfer solver, Numer. Heat Transfer Part B 32 (1997) 267–281.

[7] M. Thomadakis, M. Leschziner, A pressure-correction method for the solution of incompressible viscous flows on unstructured grids, Int. J. Numer. Methods Fluids 22 (1996) 581–601.

[8] N. Taniguchi, T. Kobayashi, Finite volume method on the unstructured grid system, Comput. Fluids 19 (1991) 287–295.

[9] M.H. Kobayashi, M.C. Pereira, J.C.F. Pereira, A conservative finite-volume second-order-accurate projection method on hybrid unstructured grids, J. Comput. Phys. 150 (1999) 40–75.

[10] J.J.H. Miller, S. Wang, An exponentially fitted finite volume method for the numerical solution of 2D unsteady incompressible flow problems, J. Comput. Phys. 115 (1994) 56–64.

[11] D. Pan, C.H. Lu, J.C. Cheng, Incompressible flow solution on unstructured triangular meshes, Numer. Heat Transfer Part B 26 (1994) 207–224.

[12] J.M. Weiss, W.A. Smith, Preconditioning applied to variable and constant density flows, AIAA J. 33 (1995) 2050–2057.

[13] K.W. Schulz, Y. Kallinderis, Unsteady flow structure interaction for incompressible flows using deformable hybrid grids, J. Comput. Phys. 143 (1998) 569–597.

[14] J.A. Chen, Y. Kallinderis, Adaptive hybrid (prismatic-tetrahedral) grid for incompressible flows, Int. J. Numer. Methods Fluids 26 (1998) 1085–1105.

[15] U. Ghia, K.N. Ghia, C.T. Shin, High-*Re* solutions for incompressible flow using the Navier–Stokes equations and a multigrid method, J. Comput. Phys. 48 (1982) 387–411.

[16] B.F. Armaly, F. Durst, J.C.F. Pereira, B. Schonung, Experimental and theoretical investigation of backward-facing step flow, J. Fluid Mech. 127 (1983) 473–496.

[17] J. Park, K. Kwon, H. Choi, Numerical solutions of flow past a circular cylinder at Reynolds numbers up to 160, KSME Int. J. 12 (1998) 1200–1205.

[18] U. Fey, M. Konig, H. Eckelmann, A new Strouhal–Reynolds-number relationship for the circular cylinder in the range $47 < Re < 2 \cdot 10^5$, Phys. Fluids 10 (1998) 1547–1549.

[19] C.H.K. Williamson, Oblique and parallel modes of vortex shedding in the wake of a circular cylinder at low Reynolds numbers, J. Fluid Mech. 206 (1989) 579–628.

[20] D. Kim, H. Choi, A second-order time-accurate finite volume method for unsteady incompressible flow on hybrid unstructured grids, J. Comput. Phys. 162 (2000) 411–428.

[21] Y.J. Jan, Finite element analysis of vortex shedding using equal order interpolations, Int. J. Numer. Methods Fluids 39 (2002) 189–211.

[22] Y. Saad, Iterative Methods for Sparse Linear Systems, PWS Publishing Co., Boston, 1996.

[23] P.A. Jayantha, I.W. Turner, A comparison of gradient approximations for use in finite-volume computational models for two-dimensional diffusion equations, Numer. Heat Transfer Part B 40 (2001) 367–390.

[24] B.R. Baliga, S.V. Patankar, A control-volume finite element method for two-dimensional fluid flow and heat transfer, Numer. Heat Transfer 6 (1983) 245–261.

[25] P. Jawahar, H. Kamath, A high-resolution procedure for Euler and Navier–Stokes computations on unstructured grids, Journal of Computational Physics 164 (2000) 165–203.

[26] H. Choi, P. Moin, J. Kim, Direct numerical simulation of turbulent flow over riblets, J. Fluid Mech. 255 (1993) 503–539.

[27] M.H. Chung, Cartesian cut cell approach for simulating incompressible flows with rigid bodies of arbitrary shape, Comput. Fluids 35 (6) (2006) 607–623, July.

[28] Y.J. Jan, A cell-by-cell thermally driven mushy-cell tracking algorithm for phase-change problems – Part I: Phase-change without natural convection, J. Comput. Mech. 40 (2) (2007) 201–216.

[29] Y.J. Jan, W.H. Sheu, A cell-by-cell thermally driven mushy-cell tracking algorithm for phase-change problem in Dendritic solidification, Numer. Heat Transfer Part B 52 (1) (2007) 69–105.

[30] Y.J. Jan, W.H. Sheu, Z.Y. Hsu, F.P. Lin, On a mushy cell tracking method for simulating Gallium melting, Numer. Heat Transfer Part B 51 (2007) 351–374.